Artificial neural network modeling of cefixime photodegradation by synthesized CoBi(2)O(4) nanoparticles

Oussama Baaloudj, Noureddine Nasrallah, Mohamed Kebir, Bouzid Guedioura, Abdeltif Amrane, Phuong Nguyen-Tri, Sonil Nanda, Aymen Amin Assadi

Artificial neural network modeling of Cefixime photodegradation by synthesized $CoBi_2O_4$ nanoparticles

Oussama Baaloudj[a], Noureddine Nasrallah[a], Mohamed Kebir[a,b], Bouzid Guedioura[c], Abdeltif Amrane[d], Phuong Nguyen-Tri[e*], Sonil Nanda[f], Aymen Amin Assadi[d*]

[a] Laboratory of Reaction Engineering, Faculty of Mechanical Engineering and Process Engineering USTHB, BP 32, Algiers, Algeria

[b] Research Unit on Analysis and Technological Development in Environment (URADTE-CRAPC), BP 384, Bou-Ismail Tipaza, Algeria

[c] Reactor division, Nuclear Research Center, Draria, Algeria

[d] Univ Rennes - ENSCR / UMR CNRS 6226 "Chemical Sciences of Rennes" ENSCR, Campus de Beaulieu, av. du Général Leclerc, 35700 Rennes, France

[e] Université du Québec à Trois-Rivières (UQTR), Trois-Rivières, Québec, G9A 5H7, Canada

[f]Department of Chemical and Biological Engineering, University of Saskatchewan, Saskatoon, Saskatchewan, S7N 5A9, Canada

* Corresponding authors: E-mail: aymen.assadi@ensc-rennes.fr (A. A. Assadi); Tel.: +33 223238152
Phuong.Nguyen-Tri@uqtr.ca (P. Nguyen-Tri); Tel : + 819 376-5011

Abstract

$CoBi_2O_4$ (CBO) nanoparticles were synthesized by sol-gel method using Polyvinylpyrrolidone (PVP) as a complexing reagent. For a single-phase with the spinel structure, the formed gel was dried and calcined at four temperatures stages. Various methods were used to identified and characterized the obtained spinel, such as X-ray diffraction (XRD), Scanning Electron Micrograph (SEM-EDX), Transmission electron microscope (TEM), Fourier transform infrared (FT-IR), X-ray fluorescence (XRF), Raman and UV-Vis spectroscopies. The photocatalytic activity of CBO was examined for the degradation of a pharmaceutical product Cefixime (CFX). Furthermore, for the prediction of the CFX degradation rate an artificial neural network model was used. The network was trained using the experimental data obtained at different pH with different CBO doses and initial CFX concentrations. To optimize the network, various algorithms and transfer functions for the hidden layer were tested. By calculating the

mean square error (MSE), 13 neurons were found to be the optimal number of neurons and produced the highest coefficient of correlation R^2 of 99.6 %. The relative significance of the input variables was calculated and the most impacting input was proved to be the initial CFX concentration. The effects of some scavenging agents were also studied. The results confirmed the dominant role of hydroxyl radical $OH^{\bullet}$ in the degradation process. With the novel $CoBi_2O_4$/ZnO hetero-system, the photocatalytic performance has been enhanced, giving an 80% degradation yield of CFX (10 mg/L) at neutral pH in only 3 hours.

Keywords: $CoBi_2O_4$ Spinel, Characterization, Cefixime, Artificial neural network, Optimization.

1. Introduction

In recent years, pharmaceutical compounds have sullied the aqueous environment, among those compounds, antibiotics are the major concern which are extremely dangerous because they are widely used in both human and veterinary medicines (Kaczala and E. Blum 2015). Antibiotics are also used to improve feed quality and thus increase rates in the poultry industries (World Health Organisation 2011). Analytical study of antibiotic use in 76 countries from 2010-2015 found that global antibiotic consumption has increased by 65% for the fifteen years studied (Sample 2018). The majority of antibiotic products are not biodegradable and their environmental contamination can increase aquatic toxicity (Mostafaloo et al. 2019). Generally, antibiotics are present at amounts ranging from ng/L to µg/L in treated wastewater (Ibáñez et al. 2017; Shokoohi et al. 2017; Mirzaei et al. 2018). But even in small amounts, the presence of these compounds in water supplies will increase bacterial resistance, which produces a kind of micro-organisms called superbugs or antibiotic resistance (ABR) that are considered to cause very dangerous health effects (Elder et al. 2020). ABR is the ability to survive and multiply in the presence of antibiotic doses that are eventually deemed effective against a bacterial population or other microorganisms (Elder et al. 2020). A statistics study indicates that antibiotic resistance causes 700,000 deaths globally each year (Liu et al. 2019). ABR is now, in the 21st century, widely recognized as a grave threat to global health ~~in the 21st century~~ (Littmann et al. 2015).

As a typical example of antibiotics, Cefixime (CFX) was chosen which belonging to broad-spectrum, third-generation cephalosporin antibiotic derived semi-synthetically from the marine fungus Cephalosporium acremonium (Shooshtari and Ghazi 2017). CFX with molecular formula $C_{16}H_{15}N_5O_7S_2$ (Fig. 1) is (6R,7R)-7-[[(2Z)-2-(2-amino -1,3-thiazol -4- yl) -2- (carboxymethoxyimino) acetyl] amino] -3- ethenyl -8- oxo -5- thia -1-azabicyclo [4.2.0] oct-2-ene-2-carboxylic acid (Sheydaei et al. 2018). A study detected CFX as one of the most prevalent antibiotics observed in different water environments with concentrations of 278.65 to 422.1 ng/L (Mirzaei et al. 2018).

Fig. 1 Molecular structure of the antibiotic Cefixime.

Most of the conventional approaches that are commonly used for the removal of antibiotics have no positive findings for the degradation of antibiotic residues from contaminated waters or have substantial inconveniences such as by-products of the degradation (Xiong et al. 2018; Zhu et al. 2018; Zhang et al. 2020). On the other hand, Advanced Oxidation Processes (AOPs) have proven to be an effective solution for the rapid degradation of non-biodegradable substances in polluted water (Lou et al. 2017; Aboudalle et al. 2018; Kamagate et al. 2018). Particularly, the Heterogeneous photocatalysis process which is one of the best approaches for aqueous environment treatment as it is safer and a natural technology (used green energy). photocatalysis has proven on a previous investigations a successful degradation for various types of pharmaceutical drugs and organic compounds in the wastewater (Kamagate et al. 2018; Nguyen et al. 2018; Li et al. 2019b; Sayadi et al. 2019). Photocatalysis is based generally on the principle of the activation of a catalyst using an energy provided by a source of light (Homem and Santos 2011). As a catalyst, semiconductors are commonly used as they are very effective and easy to synthesize. Recently, many bismuth-based semiconductors have become very significant because of their high chemical stability, their excellent ability to absorb light and its narrow optical band gap (Tho et al. 2020). Cobalt bismuthate with the chemicals formula $CoBi_2O_4$ (CBO) was chosen as a typical semiconductor. To our knowledge, only one study has dealt with the synthesis and use of CBO photocatalyst (Jagadeesh and Sailaja 2019). Moreover, no study has been made yet concerning $CoBi_2O_4$/ZnO hetero-system.

Artificial neural network (ANN) is one of the most powerful tools for modeling linear and non-linear systems (Mohammadzadeh Kakhki et al. 2020). It an effective way of predicting experimental patterns in various systems, especially for photocatalysis

(Zhou et al. 2020) Moreover, ANN has the self-learning ability and to work with incomplete knowledge, storing information on the entire network, having fault tolerance and a distributed memory (Kaur and Kaur 2014). Thus, modeling and optimization can be accomplished without the rigor of the experimental information via ANN (Ayodele et al. 2020). Owing to that, ANN has been employed in the prediction of photocatalysis CFX efficiency. The challenge in the ANN modeling is to build a network with the smallest possible number of random experimental points to modulate and achieve the expected results approach to real cases without designing an experimental model. Only a few studies have attempted this challenge (Hassani et al. 2015; Tabatabai-Yazdi et al. 2019; Zulfiqar et al. 2019). To find the most efficient and effective network, various algorithms and transfer functions for the hidden layer has been attempted.

In this study, we report the synthesis of $CoBi_2O_4$ nanoparticles which prepared by sol-gel auto combustion method using polyvinylpyrrolidone (PVP) as a complexing reagent. Various methods were used to identified and characterized the obtained spinel, such as XRD, SEM-EDX, TEM, FT-IR, XRF, Raman and UV-Vis spectroscopies. After that, Cefixime was considered as a model of antibiotic compound to tested the photocatalytic performance of this catalyst. The effect of pH, irradiation time, the concentration of CFX and concentration of catalyst on the degradation of CFX was examined and modelized using ANN. Also, a Garson formula was introduced to measure the relative significance of different input variables. After that, the effects of some scavenging agents have been studied. Finally, the new hetero-system $CoBi_2O_4$/ZnO has been tested in order to enhance the photocatalytic performance.

2. Material and methods

2.1 Chemicals

Chemicals used in the present study were bismuth nitrate pentahydrate [$Bi(NO_3)_3 \cdot 5H_2O$] (98.5% Chem-Lab), cobalt nitrate hexahydrate [$Co(NO_3)_2 \cdot 6H_2O$] (98% Biochem), Zinc nitrate hexahydrate [$N_2O_6Zn \cdot 6H_2O$] (98% Biochem), Cefixime trihydrate and Polyvinylpyrrolidone were obtained from a pharmaceutical company Pharmalliance Algeria, ethanol from Biochem, Sodium hydroxide, Hydrochloric acid, isopropanol and nitric acid were supplied by Sigma Aldrich. All chemicals were used as received without further purification. Distilled water has been used as a solvent.

2.2 Synthesis of $CoBi_2O_4$ nanoparticles

$CoBi_2O_4$ was synthesized by the aqueous PVP sol-gel method. The gel was prepared using stoichiometric amounts (1:2 ratio) of cobalt nitrate hexahydrate [$Co(NO_3)_2 \cdot 6H_2O$] and bismuth nitrate pentahydrate [$Bi(NO_3)_3 \cdot 5H_2O$] respectively. They were then dissolved in ethanol by using a magnetic stirrer; an excess of 5% citric acid was added in the solutions. After total solubilization, both solutions had been mixed and heated at 50 ºC for 1h.

In the following step, Polyvinylpyrrolidone (PVP K30), used as a complexing agent was dissolved in 50 mL water and added to the reaction solution, applied about 15% w/w to obtain the complexing role (Giannopoulou et al. 2015). After concentrating the solutions by evaporation at 80 °C under stirring, the mixed solution turned into a reddish transparent gel. After drying and combustion at 200 °C for 6 h a precursor gel powder was formed (Xerogel).

The amorphous powder was subjected to calcination at 300ºC, 400ºC, 600ºC and 800ºC in an air oven each one for 3 h. The synthesized sample was annealed to improve the degree of crystallinity and to eliminate any leftover carbonated waste after the combustion reaction. Then, it was subjected to phase identification, microstructural analysis and photocatalytic studies.

2.3 Characterization

The XRD analysis of the products was recorded by a Phillips PW 1730, X-ray diffractometer using monochromatized Cu K radiation (λ = 0.15417 nm the morphology of the sample SEM was studied using the electron scanning microscope FEI Quanta 650 equipped with EDX and Mapping analysis with 20 kV accelerated voltage. Transmission electron microscope (TEM) images of the nanostructures were taken on a JEOL-24011BU. ATR-FTIR spectra were obtained in the range of 400–4000 cm^{-1} with an Alpha Bruker spectrometer (One FTIR model). The chemical analysis was carried out by using Xray fluorescence (PANalytical epsilon3-XL spectrometer). UV–visible diffuse reflectance spectrum (DRS) of the sample was produced by dry pressed disk sample using Cary 5000 UV−vis. The Raman analysis was carried out using LabRAM HR Evolution system Horiba Jobin-Yvon.

2.4 Photocatalytic degradation study

We selected (CFX) as a pharmaceutical model contaminant to investigate $CoBi_2O_4$'s photocatalytic performance. The photocatalytic degradation of CFX was conducted by mixing an appropriate quantity of $CoBi_2O_4$ in 100 mL of CFX solution with known concentration. The pH was set to the desired value with NaOH and HCl. The solution was continuously stirred for 2h in dark conditions in a closed reactor to reach the balance of adsorption and desorption before switching on the light. As a visible light source, a tungsten bulb 200 W manufactured by Osram was applied and positioned at 10 cm from the solution surface. The intensity (8.25 mW/cm^2) and the maximum emission (630 nm) of the lamp were measured by a digital flux meter (Testo 545). A cooling system consisting of a double-walled reactor attached to a thermostatic bath (Daihan Labtech, LCB-11D) has been used to maintain the temperature of the solution nearly constant (25 ± 1 °C) during the photocatalytic experiments. At a regular time, 2 mL of the solution was centrifuged at the speed of 5,000 rpm for 10 min to filter the suspended $CoBi_2O_4$ particles from the sample and directly analyzed by UV-Visible spectrometry (OPTIZEN, UV-3220UV) at the maximum absorption wavelength of CFX (288 nm). It should be mentioned that the small positive error of UV-Visible spectrometry in comparison with HPLC was ignored. The following equation was used to calculate the degradation rate of CFX.

$$Photodegradation\% = \frac{(C_O - C)}{C_o} \times 100 \quad (1)$$

Where C_O is the initial concentration of CFX after adsorption and C is the concentration of CFX at time t.

As already mentioned, the CFX concentration was monitored by measuring the absorbance of the samples using a UV–Visible spectrophotometry. The degradation of the pollutant was followed by the disappearance of the band corresponding to CFX at 288 nm as shown in figure 2. The experiment was conducted in the presence of 0.1 g CBO at pH 6, room temperature and an initial CFX concentration of 10 mg/L.

To evaluate the CFX mineralization by the catalyst CBO, the amount of total organic carbon (TOC) in the solution at a regular time with the same conditions was measured by TOC analyzer (Shimadzu TOC-L, Japan) using the catalytic combustion

187 method at 680°C. The results of TOC analysis are presented in Fig. 2 (b). The following
188 equation was used to calculate the TOC removal (%):

$$TOC_{removal}\% = \frac{(TOC_O - TOC)}{TOC_o} \times 100 \quad (2)$$

189 where TOC_O (mg) is the initial TOC values after adsorption, TOC (mg) is the remaining
190 TOC in solution.

191 the TOC removal reached 67.23% in the presence of CBO catalyst after 6 h, which
192 confirmed that cefixime could be effectively mineralized in the presence of CBO
193 photocatalyst under visible light irradiation.

194 *Fig. 2 (a) UV–visible spectra (B)TOC removal of CFX (10 mg/L).*

195 2.5 Experimental design and modeling

196 The input layer consisted of four numbers of neurons, which are pH, irradiation
197 time (min), the dose of CBO (g/L) and concentration of CFX (mg/L), while
198 photodegradation of CFX (%) was selected as the output layer. The application was
199 performed in the laboratory to obtain the actual responses. As it is a challenge to build
200 a network with the smallest possible number of random experimental points to
201 approach to real cases without designing an experimental model. For that, a total of
202 40 random experimental points has been randomly divided into 70% training, 15%
203 testing and 15% validation data. Training data were presented to the network during
204 training. The use of validation data was to test network generalization and to stop
205 training if generalization stops. The test data provided a fully independent network
206 performance measurement during and following training (Ayoubi-Feiz et al. 2019).

207 The modeling of the photodegradation of CFX was carried out by MATLAB
208 R2014a which has been widely used (Medarević et al. 2016; Ayoubi-Feiz et al. 2019;
209 Tabatabai-Yazdi et al. 2019; Zulfiqar et al. 2019; Garg et al. 2020). The model
210 parameters are described in Table 1. For the model development, the feed-forward
211 neural network with backpropagation method was used. Furthermore, a supervised
212 learning technique called Levenberg-Marquardt with a training function ‘trainlim’ has
213 been used for training the network.

214 *Table 1 ANN model parameters.*

The number of hidden neurons is a critical element of modeling experimental processes with ANN (Hazrati et al. 2017). For its optimization, a set of topologies have been used in which the number of hidden neurons changed from 2 to 20. The mean square error MSE was performed to investigate the relation between the hidden neurons and the network error (Ayoubi-Feiz et al. 2019). The MSE function was used as Eq.3. The coefficient of correlation R (Eq.4) used to predict model conformity and applicability, the more the value is close to one, the better it is applicated.

$$MSE = \frac{1}{n}\sum_{i-1}^{n}(y_{i,NN} - y_{i,exp})^2 \quad (3)$$

$$R^2 = 1 - \frac{\sum_{i-1}^{n}(y_{i,NN} - y_{i,exp})^2}{\sum_{i-1}^{n}(y_m - y_{i,exp})^2} \quad (4)$$

where *n* is the total number of data points, $y_{i,NN}$ and $y_{i,exp}$are the network prediction and the experimental response and *i* is an index of the data, y_m is the average of the actual values.

3. Results and discussion

3.1 Characterization of the catalyst

To confirm the single phase of $CoBi_2O_4$, an X-ray diffraction (XRD) pattern after each calcination was taken. Figure 3 illustrates the effect of different annealing temperatures on the structure of the synthesized samples. The pure $CoBi_2O_4$ nano-powders were obtained at 800 °C (after annealing at 300 °C, 400 °C, 600 °C) almost a single phase of CBO without impurity was observed. The phase of the $CoBi_2O_4$ could be indexed with the five main diffraction peaks at 2θ = *27.88º (111), 33.12º (200), 45.72º (220), 52.76º (311)* and *56.04º (222)* which were in good agreement with the reference peaks (Jagadeesh and Sailaja 2019) almost the same, and also in line with the standard card (JCPDS 50-0369) from Joint Committee of Powder Diffraction Standards of the face-centered cubic of $CoBi_2O_4$.

The crystallite size was calculated from the main diffraction peaks of the last calcined product (at 800 °C) with the following Debey- Scherer formula Eq. (5). The crystalline sizes have been estimated between 19.45 and 46.39 nm.

$$D = \frac{K\lambda}{\beta\cos(\theta)} \quad (5)$$

where D is the crystallite size of the phase-in nanometers, K is the Scherrer constant. (K = 0.94 for cubic symmetry), λ is the wavelength of the X-ray beam used, β is the full width at half maxima (FWHM) in radians and θ is the Braggs angle.

Fig. 3 XRD diffractogram of $CoBi_2O_4$ calcined at (a) 300ºC, (b) 400ºC, (c) 600ºC and (d) 800ºC.

For the XRD patterns of the ZnO nanoparticles prepared via co-precipitation. As shown in Figure 4, the ZnO nanoparticles displayed a Wurtzite structure (hexagonal phase, space group P63mc). All standard peaks observed for ZnO nanoparticles were in line with those obtained from (JCPDS 36-1451) (Raou 2017).

Fig. 4 XRD diffractogram of ZnO.

The spinel structure may be considered as a continuously bound crystal in which the atoms are bonded by equivalent forces (ionic, covalent or van der Waals) to all nearest neighbors. The spinel shaped metal ions are found in two separate sub-lattices known as A-site (tetrahedral) and B-site (octahedral), as stated in the geometric arrangement of the nearest oxygen neighbors (Sabri et al. 2016). Fourier transform infrared spectra of $CoBi_2O_4$ recorded within the range of 4000–400 cm^{-1} are shown in Figure 5. It is evident in the IR spectrum that CBO had five intensive absorption peaks in the region of 400-900 cm^{-1}, which could be related to the typical metal-oxygen (M–O) vibrations (Jasaitis et al. 2011). The presence of peaks between 570 cm^{-1} and 669.9 cm^{-1} belonged to the vibration of the Bi–O bond and the vibration peak at 824.28 cm^{-1} can be assigned to Bi–O–Bi (Yang et al. 2018; Viruthagiri and Kannan 2019). Furthermore, the appearance of Peaks 446.13 cm^{-1} and 532.31 cm^{-1} can probably be related to the tetrahedral (CoO_4) in the spinel (Sousa et al. 2019).

Fig. 5 FTIR spectra of $CoBi_2O_4$.

Figure 6 shows the Raman spectra of $CoBi_2O_4$. There are five Raman-activated bands; all these modes were observed at ambient conditions. The bands above 600 cm^{-1} were due to the motion of oxygen in the tetrahedral AO_4 octahedral BO_6 groups (Li et al. 2019a), suggesting a certain amount of Co and Bi disturbance in the tetrahedral and octahedral sites. The low-frequency modes observed at 54.13, 80.5 and 123.73 cm^{-1} can be related to the Bi^{3+} ion motion in the spinel layer and the mode at 521.03 cm^{-1} can be attributed to the variation of bond distances between Bi atoms

and the spinel block apical O atoms (Zhang et al. 2018). The strongest band observed at 264 cm^{-1} corresponded to O–Bi–O vibration (Zhang and Saxena 2013). The Raman modes of 193.29, 476.05 ,600 and 670 cm^{-1} were related to the vibration of the Co atoms (Diallo et al. 2015). Besides, a small Raman band was observed at 151.35 cm^{-1}; the origin of this band is still unknown.

Fig. 6 Raman spectra of $CoBi_2O_4$.

The morphology and structures of the prepared sample were visualized by Scanning Electron Micrograph (SEM) and transmission electron microscope (TEM) techniques were used. Figure 7 (a) shows a typical SEM image of the sample. It can be observed that the sample consisted of particles exhibiting cubic morphology. Due to the ultrafine nature of the sample, these particles displayed a slightly agglomerated morphology. The TEM images of $CoBi_2O_4$ shown in figure 7 (b) demonstrate clear information regarding the size, shape and size distribution of nanoparticles. Based on the size distribution histogram in the inset figure, the catalyst was composed of particle size in the range of 22 nm. It was found that the size of the crystallite obtained from XRD analysis and the particle size obtained from TEM analysis were in the same size order. This picture also shows the existence of several aggregations within the range of nanometres.

The electron diffraction pattern of the nanoparticles are shown in figure 7 c, This pattern has a cubic shape and right angles (K/H = 1, $(\vec{H},\vec{K})$ = 90°) which is defined as a cubic face-centered CFC type of crystalline spinel (Andrews KW , Dyson DJ 1967) and that confirmed the XRD results.

Fig. 7 SEM (a) TEM (b) Diffraction pattern (c) of nanoparticles $CoBi_2O_4$.

The elementary study of the $CoBi_2O_4$ nanoparticles was carried out by Energy Dispersive X-ray spectrometer (EDX). The peaks for Co, Bi and O elements were clearly observed in the EDX image, as shown in figure 8 (a). The atomic percentage of the elements in the sample are given in the inset Table of the EDX data. The atomic percentages of Co, Bi and O were estimated to be 14.02%, 26.25% and 59.73%, respectively. The quantification of Co, Bi and O confirmed that the atomic ratio of Co:Bi:O was 1.00:1.87:4.26, which agrees with the theoretical stoichiometric composition of $CoBi_2O_4$.

X-ray fluorescence measurements (XRF) spectra figure 8 (b) showed that Co and Bi were the most abundant elements. Regarding silver (Ag), it was used in the XRF analysis method. The inset Table of the XRF results shows that the weight percentage of CoO and Bi_2O_3 was estimated to be (14.109%) for CoO and (85.89%) Bi_2O_3. The molar mass was then calculated for CoO and Bi_2O_3 and found to be 74.93 and 467.96 g/mol, respectively. This confirmed that the atomic ratio of Co:Bi:O was 1.00:1.95:3.93, which agrees with the theoretical stoichiometric composition of $CoBi_2O_4$ and also in line with the EDX analysis.

Fig. 8 Energy dispersive X-ray (a) X-ray fluorescence (b) diffractogram of nanoparticles $CoBi_2O_4$.

The elemental mappings in figure 9 were located in the same EDX region. The colored map of the SEM image (where Co, Bi and O are given in colors like Green, Red and Blue, respectively) revealed that Co, Bi, and O elements coexisted and were uniformly distributed.

Fig. 9 EDX elemental mapping images of $CoBi_2O_4$ a) All elements b) Cobalt c) Bismuth d) Oxygen.

Optical properties of $CoBi_2O_4$ nanostructure were measured using the UV–Vis diffuse reflectance spectrum. As shown in figure 10, the bandgap was estimated as 2.5 eV which is lower than that of TiO_2 and ZnO (3.2 eV) (Serpone 2006; Miki-yoshida 2016). This indicates that CBO has an excellent absorption level in the wavelength range from 300 to 800 nm that contains both UV and visible light, which appears more efficient than ZnO and TiO_2, leading to an increase in the formation of electron-hole pairs on the photocatalyst's surface in visible light irradiation.

Fig. 10 UV–Vis optical absorption edges.

3.2 Artificial neural network modeling of the elimination of Cefixime

For the modeling, irradiation time, pH, initial CFX concentration and CBO catalyst dose were selected as the input variables and the related degradation rate of CFX was the output variable. To feed the structure of the ANN, a total of 40 experimental sets were used. The data sets have been divided into 70% training, 15% validation and 15% test, as shown in Table 2.

Table 2 Data sets of experimental results and ANN's predicted results.

The essential part of the neural network architecture is the choice of the number of hidden neurons. The model's best performance comes when the mean square error (MSE) determined using equation (2), is the smallest.

Fig. 11 Impact of the number of hidden neurons on the MSE of the neural network.

Figure 11 shows that the Levenberg-Marquardt with a training function 'trainlim' and 13 hidden-layer neurons produced the highest correlation coefficient $R^2 = 0.996$ and the smallest MSE value 1.81×10^{-4}. The relation of experimental data to ANN model predictions can be derived from the contrast between the experimental data and the predictions of the ANN model (Fig.12). The training data were given as the model's input values, and the simulation output was compared with the relevant experimental data. The adaptation of the model results to experimental data for the training data set was very successful. The main part of model validation is the testing of network performance for the testing data set access, the correlation coefficient was likewise very high in this case $R^2_{\text{test}} = 0.977$.

Fig. 12 The relation of experimental data to the ANN model's predictions for each type of data.

3.2.1 Effect of pH

The pharmaceuticals polluted water is discharged in the environment at variable pH values; consequently, it is necessary to investigate the role of pH on the photocatalytic degradation. For this purpose, photodegradation experiments have been carried out in 100 ml of 10 mg/L CFX solution at a fixed CBO amount of 0.1 g and 360 min irradiation. Three different initial pH was selected and kept constant by adding HCl or NaOH. The degradation rate of CFX increased with the increase of the pH value of the solution from 4 to 6 and then decreased from 6 to 8, as observed in figure 13 (a). Based on these results, it can be deduced that the photodegradation of CFX was optimal at pH = 6. It is difficult to grasp pH impact on the performance of the photocatalytic degradation process because of its multiple roles, such as the neutral electrical charge of the CFX molecules, as well as the protonation and the electropositive surface of CBO. This may also be related to the reaction between organic compounds and dissolved oxygen (Abbasi and Hasanpour 2017). The improvement of the photocatalytic activity of the catalyst at pH = 6 can probably be related to the charge accumulation on the external surface (Bai et al. 2017). So, the

pH change may therefore affect the dispersion of the catalyst in the suspension. Moreover, figure 13 (b) shows that the values predicted by the ANN model were well in line with the experimental data.

3.2.2 Effect of the catalyst dose

The effect of CBO catalyst dose on the photodegradation activity of CFX was examined. A set experiment was conducted by using a catalyst dose ranging from 0.05 to 0.15 g in 100 mL of solution for 15 mg/L of CFX at pH = 6 and 360 min irradiation. Figure 13 (c) illustrates the effect of the catalyst dose on the CFX photodegradation removal, showing that the degradation of CFX increased from 66% to 72% for an increase of the catalyst dose from 0.05 to 0.08 g because of the limited active sites available on the CBO catalyst surface. However, the degradation efficiency of CFX decreased beyond this amount of catalyst, namely from 0.08 to 0.15 g. This may be attributed to the fact that the accumulation of free catalysts leads to an increase in the opacity of the solution and a decrease in light penetration. This is due to a scattering effect for an expansion of the dose of catalyst (Zhou et al. 2018). Therefore, the optimal dosage of the catalyst for CFX photodegradation was selected to be 0.08 g. Based on the obtained results shown in figure 13 (d), the results predicted by the ANN and the experimental values were well agreed.

3.2.3 Effect of the initial CFX concentration

For the purpose, the photodegradation studies were performed by varying initial concentrations of CFX from 5 to 15 mg/L in 100 ml of the solution with 0.1 g of the CBO catalyst at pH 6 after 360 min of irradiation time under visible light. Figure 13 (e) shows that by raising the CFX concentration, the degradation yield decreased from 82 to 55%. This behavior can be related to the diminishing number of available sites on the catalyst CBO surface. Therefore, a high number of CFX molecules would have an inhibitory effect on the photodegradation efficiency due to the lack of any direct contact between the CBO catalyst surface and CFX. Besides, many photons could be absorbed by the CFX molecules and hence did not reach the catalyst surface. The comparison between ANN predicted values and the experimental data shown in figure 13 (f) revealed a good agreement between them.

Fig. 13 (a) effect pH (c) effect of catalyst dose (e) effect of initial CFX concentration (b,d,f) Comparison of the experimental results with the predicted ANN values for various operating parameters.

3.2.4 The relative significance

An evaluation process based on the network weight matrix and the Garson's equation (Garson 1991) was applied to calculate the relative significance of the input variables on the network's output. The relative significance of input variables influencing the CFX photodegradation values has been calculated by equation 6 (Ibrahim 2013).

$$RI_X = \sum_{x=1}^{n} \frac{\left|w_{xy} w_{yz}\right|}{\sum_{y=1}^{m} \left|w_{xy} w_{yz}\right|} \quad (6)$$

where RI_X is the relative significance, n and m are respectively the input numbers and hidden neurons. w_{xy} are the connection weights, $\sum_{y=1}^{m} \left|w_{xy} w_{yz}\right|$ is the sum of the product of the final weights of the connections from input neurons to hidden neurons along with the links from hidden neurons to output neurons (Ibrahim 2013).

Table 3 ANN model's weight and bias matrix.

The ANN model's weight matrix is given in Table 3, while the relative significance of the input variables derived from equation (4) is displayed in figure 14. As can be seen, the initial CFX concentration showed the most significant impact on the performance of CFX photodegradation (28%) compared with the other operating factors, namely CBO dosage (27%), irradiation time (24%) and pH (21%).

Fig. 14 The relative significance of the inputs on CFX degradation.

3.3 Effect of scavenging agents and the photocatalytic mechanism

Generally, the photodegradation of organic compounds by a catalyst semi-conductor can be described by different reaction pathways regulated by different active species such as $OH^{\bullet}$ hydroxyl radical, superoxide $O_2^{\bullet}$, and photogenerated electrons and holes e^-/ h^+ pairs which called reactive oxidant species (ROS) (Zuo et al. 2017). To investigate the dominant ROS on the photodegradation of Cefixime over the CBO catalyst and for an understanding of the photocatalytic mechanism, several active species trapping tests were run in the presence of different concentrations of some

scavengers. Each of the scavenging species was chosen for a specific type of photocatalytic radicals. p-Benzoquinone BQ was used as superoxide $O_2^{\bullet}$ radical quencher (a scavenger for superoxide anion radical) (Nithya and Ayyappan 2020), Potassium dichromate $K_2Cr_2O_7$ was used as a scavenger for electron (e^-) (Gupta et al. 2020), Disodium ethylenediaminetetraacetic acid (Na_2-EDTA) was used as a scavenger for the hole (h^+) and as photoinduced h^+ acceptor (Tho et al. 2020) and isopropanol (IPA) alcohol was employed as an $OH^{\bullet}$ scavenger (hydroxyl $OH^{\bullet}$ radical quencher) (Ghattavi and Nezamzadeh-Ejhieh 2020). The tests were performed with an initial Cefixime concentration of 5 mg/L, at pH 6, and using CBO with a solution ratio of 0.8 g/L. The impact of these scavenging agents (quenchers) on the photodegradation efficiency of CBO nanocomposite was shown in Fig 15.

Fig. 15 Effect of different scavengers on photocatalytic degradation of CFX over CBO photocatalyst.

The obtained results are summarized in the next order of the photodegradation efficiency in the presence of different scavengers: Sample without the scavengers (Free) (79 %) > $K_2Cr_2O_7$ (64%) > p-Benzoquinone (59%) > Na_2-EDTA (40%) > Isopropanol (25%). As shown, the most decrease in the degradation efficiency was observed by Isopropanol which confirmed that the generated $OH^{\bullet}$ has a dominant role in the degradation of CFX. $OH^{\bullet}$ radicals are strong, active and unselected oxidizing species for organic substrates in terms of oxidative degradation (Kumar et al. 2020). Then it comes Na_2-EDTA, this indicates that both $OH^{\bullet}$ and h^+ are the major active species. However, in the presence of p-Benzoquinone, only a small effect has been observed on the CFX photodegradation. This indicates that $O_2^{\bullet}$ was a minor active species. The effect of $K_2Cr_2O_7$ was so small that it neglected the electron e^- role in the CFX degradation. According to these results, the following pathways (Fig. 16 and equations 7,8,9 and 10) were suggested for the photodegradation of CFX onto CBO.

$$CoBi_2O_4 + hv \rightarrow CoBi_2O_4{}^* + e^- + h^+ \quad (7)$$

$$H_2O + h^+ \rightarrow OH^* + H^+ \quad (8)$$

$$O_2 + e^- \rightarrow O_2{}^{-*} \quad (9)$$

$$CFX + OH^* + h^+ + O_2{}^{-*} \rightarrow CO_2 + H_2O + other\ small\ \text{degradation products} \quad (10)$$

Fig. 16 Proposed mechanism for CFX degradation in the presence of $CoBi_2O_4$ nanoparticles.

3.4 Comparison of Cefixime photodegradation by different processes

In order to enhance the photocatalytic performance of CFX by synthesized CBO nanoparticles and also to eliminate the photolysis effect, a set of experiments have been tested in the same condition as illustrated in fig.17. The experiment was conducted in the presence of 0.1 g catalyst at pH 6, room temperature and an initial CFX concentration of 10 mg/L. In the absence of the catalyst, a very small degradation rate of CFX by photolysis can be observed, lower than 5%. On the other hand, in the presence of the CBO photocatalyst, the degradation rate of CFX reached 60 % within 3 h. The hetero-systems can increase the rate of photo-activity by extending the spectral photo response of wide band semiconductors toward the visible light region, as already demonstrated in recent works (Belaissa et al. 2016; Boumaza et al. 2016; Rekhila et al. 2017; Boutra et al. 2019). For that, the new hetero-system $CoBi_2O_4$/ZnO has been tested. Different weight ratios of the two catalysts CBO and ZnO were tested to examine the impact on the CFX photodegradation. As can be seen in fig.17, the high photodegradation efficiency was noticed at ratio of 50%/50% weight percentage of the hetero-system $CoBi_2O_4$/ZnO, leading to an 80% degradation efficiency within only 3 h.

Fig. 17 Time-course of the CFX degradation by different processes.

4. Conclusion

In summary, in the present work, $CoBi_2O_4$ nanoparticles were successfully synthesized by the sol-gel method and then characterized by both spectroscopic and morphological tools. The catalysts prepared were tested for CFX antibiotic degradation. The photocatalytic degradation of CFX was modeled successfully using an artificial neural network (ANN). A feed-forward neural network with backpropagation method and a Levenberg-Marquardt method was used. The degradation of CFX in different operating conditions was predicted with 13 hidden neurons. The results showed that the $CoBi_2O_4$ nanoparticles led to an 86 % CFX photodegradation yield in the following optimal condition, pH = 6, 5 mg/L CFX, 0.8 g/L catalyst dose and 360 min of irradiation. It was shown that all the parameters of the study (irradiation time, pH, initial concentration of CFX and catalyst dose) have a significant effect on the CFX photodegradation.

However, the main effect was the CFX's initial concentration. Moreover, the effects of some scavenging agents were studied and the results confirmed the dominant role

of hydroxyl radical OH• in the CFX degradation process. Finally, the new $CoBi_2O_4$/ZnO hetero-system was discussed and demonstrated a rapid degradation efficiency of 80 % in just 3 hours. Owing to these promising preliminary results, it will be further considered in future works.

Acknowledgment

The authors gratefully acknowledge the financial support from the Thematic Research Agency for Science and Technology (ATRST) through the national research program (PM, PRFU Project N°A16N01UN160420190002) and the Directorate-General for Scientific Research and Technological Development (DGRSDT) of Algeria.

Declaration

Ethics approval and consent to participate

Not applicable

Consent for publication

Not applicable

Competing interest

The authors declare that they have no conflict of interest.

Authors contributions

Oussama Baaloudj and Mohamed Kebir: investigation, formal analysis, visualization, writing original draft.

Noureddine Nasrallah and Aymen Amin Assadi: conceptualization, funding acquisition, methodology, resources, project administration, supervision, writing-review and editing.

Phuong Nguyen-Tri: writing-review and editing, methodology, conceptualization.

Bouzid Guedioura: formal analysis

Abdeltif Amrane and Sonil Nanda: investigation, visualization.

Availability of data and materials:

The datasets used and/or analysed during the current study are available from the corresponding author on reasonable request.

References

Abbasi S, Hasanpour M (2017) The effect of pH on the photocatalytic degradation of methyl orange using decorated ZnO nanoparticles with SnO2 nanoparticles. J Mater Sci Mater Electron 28:1307–1314. https://doi.org/10.1007/s10854-016-5660-5

Aboudalle A, Fourcade F, Assadi AA, et al (2018) Reactive oxygen and iron species monitoring to investigate the electro-Fenton performances. Impact of the electrochemical process on the biodegradability of metronidazole and its by-products. Chemosphere 199:486–494. https://doi.org/10.1016/j.chemosphere.2018.02.075

Andrews KW , Dyson DJ KS (1967) Interpretation of electron diffraction patterns

Ayodele BV, Alsaffar MA, Mustapa SI, Vo DVN (2020) Backpropagation neural networks modelling of photocatalytic degradation of organic pollutants using TiO2-based photocatalysts. J Chem Technol Biotechnol. https://doi.org/10.1002/jctb.6407

Ayoubi-Feiz B, Sheydaei M, Karimi M (2019) Visible light photoelectrocatalysis for wastewater treatment using bifacial N-TiO2/Graphene/Ho2O3/Titanium nanocomposite: Artificial neural network modeling and evaluation of ozone addition. Process Saf Environ Prot 127:56–65. https://doi.org/10.1016/j.psep.2019.04.026

Bai Y, Huang H, Wang C, et al (2017) Engineering the surface charge states of nanostructures for enhanced catalytic performance. Mater Chem Front 1:1951–1964. https://doi.org/10.1039/c7qm00020k

Diallo A, Beye AC, Doyle TB, et al (2015) Green synthesis of Co3O4 nanoparticles via Aspalathus linearis: Physical properties. Green Chem Lett Rev 8:30–36. https://doi.org/10.1080/17518253.2015.1082646

Elder FCT, Feil EJ, Snape JN, et al (2020) The role of stereochemistry of antibiotic

546 agents in the development of antibiotic resistance in the environment. Environ Int
547 139:105681. https://doi.org/10.1016/j.envint.2020.105681

548 Garg A, Kaur G, Sangal VK, et al (2020) Optimization methodology based on neural
549 networks and box - behnken design applied to photocatalysis of acid red. 0–2.
550 https://doi.org/10.4491/eer.2019.246

551 Garson GD (1991) Interpreting neural-network connection weights. AI Expert 6:46–51

552 Ghattavi S, Nezamzadeh-Ejhieh A (2020) A visible light driven AgBr/g-C3N4
553 photocatalyst composite in methyl orange photodegradation: Focus on
554 photoluminescence, mole ratio, synthesis method of g-C3N4 and scavengers.
555 Compos Part B Eng 183:107712.
556 https://doi.org/10.1016/j.compositesb.2019.107712

557 Giannopoulou I, Saïs F, Thomopoulos R (2015) Handbook-of-pharmaceutical-
558 excipients-6th-edition. Rev des Nouv Technol l'Information E.28:257–262

559 Gupta NK, Ghaffari Y, Kim S, et al (2020) Photocatalytic Degradation of Organic
560 Pollutants over MFe2O4 (M = Co, Ni, Cu, Zn) Nanoparticles at Neutral pH. Sci
561 Rep 10:1–11. https://doi.org/10.1038/s41598-020-61930-2

562 Hassani A, Khataee A, Karaca S (2015) Photocatalytic degradation of ciprofloxacin
563 by synthesized TiO2 nanoparticles on montmorillonite: Effect of operation
564 parameters and artificial neural network modeling. J Mol Catal A Chem 409:149–
565 161. https://doi.org/10.1016/j.molcata.2015.08.020

566 Hazrati H, Moghaddam AH, Rostamizadeh M (2017) The influence of hydraulic
567 retention time on cake layer specifications in the membrane bioreactor:
568 Experimental and artificial neural network modeling. J Environ Chem Eng
569 5:3005–3013. https://doi.org/10.1016/j.jece.2017.05.050

570 Homem V, Santos L (2011) Degradation and removal methods of antibiotics from
571 aqueous matrices - A review. J Environ Manage 92:2304–2347.
572 https://doi.org/10.1016/j.jenvman.2011.05.023

573 Ibáñez M, Borova V, Boix C, et al (2017) UHPLC-QTOF MS screening of
574 pharmaceuticals and their metabolites in treated wastewater samples from
575 Athens. J Hazard Mater 323:26–35.

https://doi.org/10.1016/j.jhazmat.2016.03.078

Ibrahim OM (2013) A comparison of methods for assessing the relative importance of input variables in artificial neural networks. J Appl Sci Res 9:5692–5700. https://doi.org/10.1067/mmt.2002.123333

Jagadeesh C, Sailaja BB V (2019) Photocatalytic Degradation of Rohdamine B Dye using CoBi2O4 Nanocatalyst and Effect of Various Operational Parameters. CIKITUSI J 6:97–107

Jasaitis D, Beganskiene A, Senvaitiene J, et al (2011) Sol-gel synthesis and characterization of cobalt chromium spinel CoCr 2O 4. Chemija 22:125–130. https://doi.org/10.1039/c3ce41663a

Kaczala F, E. Blum S (2015) The Occurrence of Veterinary Pharmaceuticals in the Environment: A Review. Curr Anal Chem 12:169–182. https://doi.org/10.2174/1573411012666151009193108

Kamagate M, Amin Assadi A, Kone T, et al (2018) Activation of persulfate by irradiated laterite for removal of fluoroquinolones in multi-component systems. J Hazard Mater 346:159–166. https://doi.org/10.1016/j.jhazmat.2017.12.011

Kaur R, Kaur B (2014) Artificial Neural Network Learning Enhancement using Bacterial Foraging Optimization Algorithm. Int J Comput Appl 102:27–33. https://doi.org/10.5120/17852-8812

Kumar R, Barakat MA, Al-Mur BA, et al (2020) Photocatalytic degradation of cefoxitin sodium antibiotic using novel BN/CdAl2O4 composite. J Clean Prod 246:119076. https://doi.org/10.1016/j.jclepro.2019.119076

Li K, Luo Y, Liu B, et al (2019a) High-performance NO2-gas sensing of ultrasmall ZnFe2O4 nanoparticles based on surface charge transfer. J Mater Chem A 7:5539–5551. https://doi.org/10.1039/c8ta12168k

Li Q, Jia R, Shao J, He Y (2019b) Photocatalytic degradation of amoxicillin via TiO2 nanoparticle coupling with a novel submerged porous ceramic membrane reactor. J Clean Prod 209:755–761. https://doi.org/10.1016/j.jclepro.2018.10.183

Littmann J, Buyx A, Cars O (2015) Antibiotic resistance: An ethical challenge. Int J Antimicrob Agents 46:359–361. https://doi.org/10.1016/j.ijantimicag.2015.06.010

606 Liu M, Ni H, Yang L, et al (2019) Pretreatment of swine manure containing β-lactam
607 antibiotics with whole-cell biocatalyst to improve biogas production. J Clean Prod
608 240:118070. https://doi.org/10.1016/j.jclepro.2019.118070

609 Lou W, Kane A, Wolbert D, et al (2017) Study of a photocatalytic process for removal
610 of antibiotics from wastewater in a falling film photoreactor: Scavenger study and
611 process intensification feasibility. Chem Eng Process Process Intensif 122:213–
612 221. https://doi.org/10.1016/j.cep.2017.10.010

613 Medarević DP, Kleinebudde P, Djuriš J, et al (2016) Combined application of mixture
614 experimental design and artificial neural networks in the solid dispersion
615 development. Drug Dev Ind Pharm 42:389–402.
616 https://doi.org/10.3109/03639045.2015.1054831

617 Miki-yoshida M (2016) Optical Band Gap Estimation of ZnO Nanorods a E = B ^ E -
618 Eg h. 19:33–38. https://doi.org/10.1590/1980-5373-mr-2015-0612

619 Mirzaei R, Yunesian M, Nasseri S, et al (2018) Occurrence and fate of most
620 prescribed antibiotics in different water environments of Tehran, Iran. Sci Total
621 Environ 619–620:446–459. https://doi.org/10.1016/j.scitotenv.2017.07.272

622 Mohammadzadeh Kakhki R, Mohammadpoor M, Faridi R, Bahadori M (2020) The
623 development of an artificial neural network-genetic algorithm model (ANN-GA)
624 for the adsorption and photocatalysis of methylene blue on a novel sulfur-
625 nitrogen co-doped Fe2O3 nanostructure surface. RSC Adv 10:5951–5960.
626 https://doi.org/10.1039/c9ra10349j

627 Mostafaloo R, Mahmoudian MH, Asadi-ghalhari M (2019) BiFeO 3 / Magnetic
628 nanocomposites for the photocatalytic degradation of ce fi xime from aqueous
629 solutions under visible light. J Photochem Photobiol A Chem 382:111926.
630 https://doi.org/10.1016/j.jphotochem.2019.111926

631 Nguyen CH, Fu CC, Juang RS (2018) Degradation of methylene blue and methyl
632 orange by palladium-doped TiO2 photocatalysis for water reuse: Efficiency and
633 degradation pathways. J Clean Prod 202:413–427.
634 https://doi.org/10.1016/j.jclepro.2018.08.110

635 Nithya R, Ayyappan S (2020) Novel exfoliated graphitic-C3N4 hybridised ZnBi2O4
636 (g-C3N4/ZnBi2O4) nanorods for catalytic reduction of 4-Nitrophenol and its

637 antibacterial activity. J Photochem Photobiol A Chem 398:.
638 https://doi.org/10.1016/j.jphotochem.2020.112591

639 Raou D (2017) Synthesis and microstructural properties of ZnO nanoparticles
640 prepared by precipitation method Synthesis and microstructural properties of
641 ZnO nanoparticles prepared by precipitation method. Renew Energy 50:932–
642 937. https://doi.org/10.1016/j.renene.2012.08.076

643 Sabri K, Rais A, Taibi K, et al (2016) Structural Rietveld refinement and vibrational
644 study of MgCrxFe2−xO4 spinel ferrites. Phys B Condens Matter 501:38–44.
645 https://doi.org/10.1016/j.physb.2016.08.011

646 Sample I (2018) Calls to rein in antibiotic use after study shows 65% increase
647 worldwide. In: Guard. https://www.theguardian.com/science/2018/mar/26/calls-
648 to-rein-in-antibiotic-use-after-study-shows-65-increase-worldwide. Accessed 26
649 Mar 2018

650 Sayadi MH, Sobhani S, Shekari H (2019) Photocatalytic degradation of azithromycin
651 using GO@Fe3O4/ ZnO/ SnO2 nanocomposites. J Clean Prod 232:127–136.
652 https://doi.org/10.1016/j.jclepro.2019.05.338

653 Serpone N (2006) Is the band gap of pristine TiO2 narrowed by anion- and cation-
654 doping of titanium dioxide in second-generation photocatalysts? J Phys Chem B
655 110:24287–24293. https://doi.org/10.1021/jp065659r

656 Sheydaei M, Shiadeh HRK, Ayoubi-Feiz B, Ezzati R (2018) Preparation of nano N-
657 TiO2/graphene oxide/titan grid sheets for visible light assisted photocatalytic
658 ozonation of cefixime. Chem Eng J 353:138–146.
659 https://doi.org/10.1016/j.cej.2018.07.089

660 Shokoohi R, Leili M, Dargahi A, et al (2017) Common Antibiotics in Wastewater of
661 Sina and Besat Hospitals, Hamadan, Iran. Arch Hyg Sci 6:152–159.
662 https://doi.org/10.29252/archhygsci.6.2.152

663 Shooshtari NM, Ghazi MM (2017) An investigation of the photocatalytic activity of
664 nano A-Fe2O3/ZnO on the photodegradation of cefixime trihydrate. Chem Eng J
665 315:527–536. https://doi.org/10.1016/j.cej.2017.01.058

666 Sousa OM, Lima JS, Lima AF, Lalic M V. (2019) Theoretical study of structural,

667 electronic and magnetic properties of the spinel Co 3 O 4 under the pressure
668 from 0 to 30 GPa. J Magn Magn Mater 484:21–30.
669 https://doi.org/10.1016/j.jmmm.2019.03.122

670 Tabatabai-Yazdi FS, Ebrahimian Pirbazari A, Esmaeili Khalilsaraei F, et al (2019)
671 Photocatalytic treatment of tetracycline antibiotic wastewater by silver/TiO2
672 nanosheets/reduced graphene oxide and artificial neural network modeling.
673 Water Environ Res. https://doi.org/10.1002/wer.1258

674 Tho NTM, Khanh DNN, Thang NQ, et al (2020) Novel reduced graphene
675 oxide/ZnBi2O4 hybrid photocatalyst for visible light degradation of 2,4-
676 dichlorophenoxyacetic acid. Environ Sci Pollut Res 27:11127–11137.
677 https://doi.org/10.1007/s11356-020-07752-1

678 Viruthagiri G, Kannan P (2019) Visible light mediated photocatalytic activity of cobalt
679 doped Bi 2 O 3 nanoparticles. J Mater Res Technol 8:127–133.
680 https://doi.org/10.1016/j.jmrt.2017.06.011

681 World Health Organisation (2011) Tackling antibiotic resistance from a food safety
682 perspective in Europe. World Heal Organ 1–88

683 Xiong W, Zeng G, Yang Z, et al (2018) Adsorption of tetracycline antibiotics from
684 aqueous solutions on nanocomposite multi-walled carbon nanotube
685 functionalized MIL-53(Fe) as new adsorbent. Sci Total Environ 627:235–244.
686 https://doi.org/10.1016/j.scitotenv.2018.01.249

687 Yang J, Xie T, Liu C, Xu L (2018) Facile fabrication of dumbbell-like β-Bi2O3/
688 graphene nanocomposites and their highly efficient photocatalytic activity.
689 Materials (Basel) 11:. https://doi.org/10.3390/ma11081359

690 Zhang FX, Saxena SK (2013) Raman studies of Bi 2 Cu O 4 at high pressures.
691 141926:2–5. https://doi.org/10.1063/1.2189450

692 Zhang H, Ke H, Ying P, et al (2018) Crystallisation process of Bi5Ti3FeO15
693 multiferroic nanoparticles synthesised by a sol–gel method. J Sol-Gel Sci
694 Technol 85:132–139. https://doi.org/10.1007/s10971-017-4530-9

695 Zhang X, Zhang Y, Ngo HH, et al (2020) Characterization and sulfonamide antibiotics
696 adsorption capacity of spent coffee grounds based biochar and hydrochar. Sci

Total Environ 716:. https://doi.org/10.1016/j.scitotenv.2020.137015

Zhou C, Wang Q, Zhou C (2020) Photocatalytic degradation of antibiotics by molecular assembly porous carbon nitride: Activity studies and artificial neural networks modeling. Chem Phys Lett 750:137479. https://doi.org/10.1016/j.cplett.2020.137479

Zhou F, Yan C, Liang T, et al (2018) Photocatalytic degradation of Orange G using sepiolite-TiO2 nanocomposites: Optimization of physicochemical parameters and kinetics studies. Chem Eng Sci 183:231–239. https://doi.org/10.1016/j.ces.2018.03.016

Zhu H, Chen T, Liu J, Li D (2018) Adsorption of tetracycline antibiotics from an aqueous solution onto graphene oxide/calcium alginate composite fibers. RSC Adv 8:2616–2621. https://doi.org/10.1039/c7ra11964j

Zulfiqar M, Samsudin MFR, Sufian S (2019) Modelling and optimization of photocatalytic degradation of phenol via TiO2 nanoparticles: An insight into response surface methodology and artificial neural network. J Photochem Photobiol A Chem 384:112039. https://doi.org/10.1016/j.jphotochem.2019.112039

Zuo S, Chen Y, Liu W, et al (2017) A facile and novel construction of attapulgite/Cu2O/Cu/g-C3N4 with enhanced photocatalytic activity for antibiotic degradation. Ceram Int 43:3324–3329. https://doi.org/10.1016/j.ceramint.2016.11.173

Table 1 ANN model parameters.

Parameters	Value
Input Neurons	pH, time, dose CBO, concentration of CFX
Output Neurons	Degradation of CFX
Number of Hidden Layer	(2-20) selection based on minimum MSE
Training function	Levenberg-Marquardt
Number experiment points	40 points
Performance function	MSE
Data division	70%-15%-15%

Table 2 Data sets of experimental results and ANN's predicted results.

Run	Time (min)	pH	CFC (ppm)	photocatalyst (g/l)	photodegradation (%)	
					Actual	Predicted
1	30	6	10	1	0.1281	0.1303
2	360	6	15	1	0.5471	0.5501
3	120	6	10	1	0.4812	0.4831
4	30	6	15	0.75	0.1065	0.1087
5	240	6	10	1	0.6813	0.6816
6	240	6	12.5	1	0.5814	0.5742
7	360	6	10	1	0.7031	0.699
8	60	6	15	1.5	0.1238	0.1229
9	240	4	10	1	0.5378	0.5382
10	300	8	10	1	0.6216	0.6205
11	360	8	10	1	0.6445	0.6484
12	300	6	15	1.5	0.4857	0.4864
13	180	4	10	1	0.4538	0.454
14	300	6	15	0.75	0.5017	0.5027
15	60	4	10	1	0.1387	0.1403
16	120	6	15	1.5	0.2286	0.2286
17	360	4	10	1	0.5588	0.5753
18	120	6	15	0.5	0.3464	0.3529
19	360	6	15	1.5	0.5238	0.5521
20	60	6	12.5	1	0.2093	0.2002
21	180	6	15	0.5	0.3954	0.4005
22	120	6	15	1	0.3134	0.3162
23	120	6	15	0.75	0.3471	0.3442
24	360	6	15	0.5	0.4444	0.4585
25	300	6	15	0.5	0.45	0.4448
26	360	6	15	0.75	0.502	0.504
27	300	6	15	1	0.538	0.5336
28	60	8	10	1	0.1972	0.1965
29	60	6	15	1	0.183	0.1828
30	180	8	10	1	0.4954	0.4832
31	60	6	5	1	0.4468	0.4464
32	300	4	10	1	0.5588	0.5592
33	240	6	15	1	0.4928	0.503
34	30	6	5	1	0.1844	0.282
35	240	6	5	1	0.8227	0.8208
36	300	6	10	1	0.6969	0.7056
37	360	6	5	1	0.8227	0.824
38	180	6	10	1	0.6	0.6174
39	60	6	15	0.5	0.2647	0.2456
40	60	6	10	1	0.2469	0.2497

Table 3 ANN model's weight and bias matrix.

Neurons of hidden layer	Weights and biases between input and hidden layers					Weights and biases between hidden and output layers	
	Input variables				Bias	Output Degradation Rate %	Bias
	Radiation time	pH	Initial concentration of CFX	Catalyst dosage			
1	-0.209	-0.155	-2.371	-1.364	2.586	0.258	
2	-0.524	-1.142	-1.34	-1.544	2.318	-0.514	
3	-1.669	1.438	1.281	-1.376	1.922	0.081	
4	1.204	1.295	-1.615	0.709	-0.558	0.515	
5	-1.58	0.183	1.387	-1.792	1.284	0.217	
6	-1.005	-1.551	-1.256	1.273	0.359	0.117	
7	1.407	-1.721	-0.843	-0.515	-0.531	-0.157	-0.29
8	-0.0028	-1.191	-1.811	-0.459	-0.645	0.3	
9	-1.107	-1.116	-0.201	-1.503	-0.872	-0.277	
10	-0.5608	1.804	-0.763	1.813	-1.227	-0.721	
11	2.053	0.782	-0.303	-0.83	1.619	0.71	
12	1.637	-0.136	-1.36	-1.151	2.809	-0.614	
13	1.435	0.1417	-1.93	-1.541	2.271	0.231	

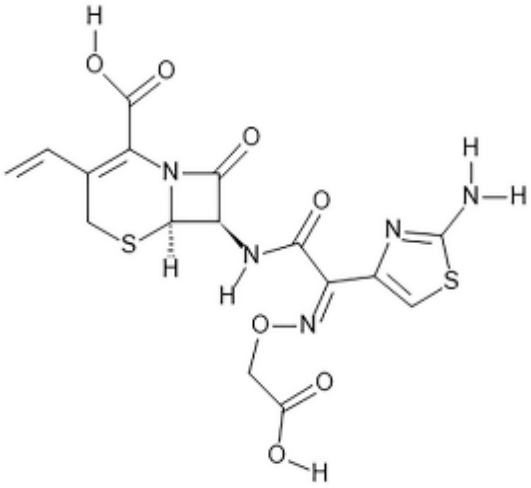

Fig. 1

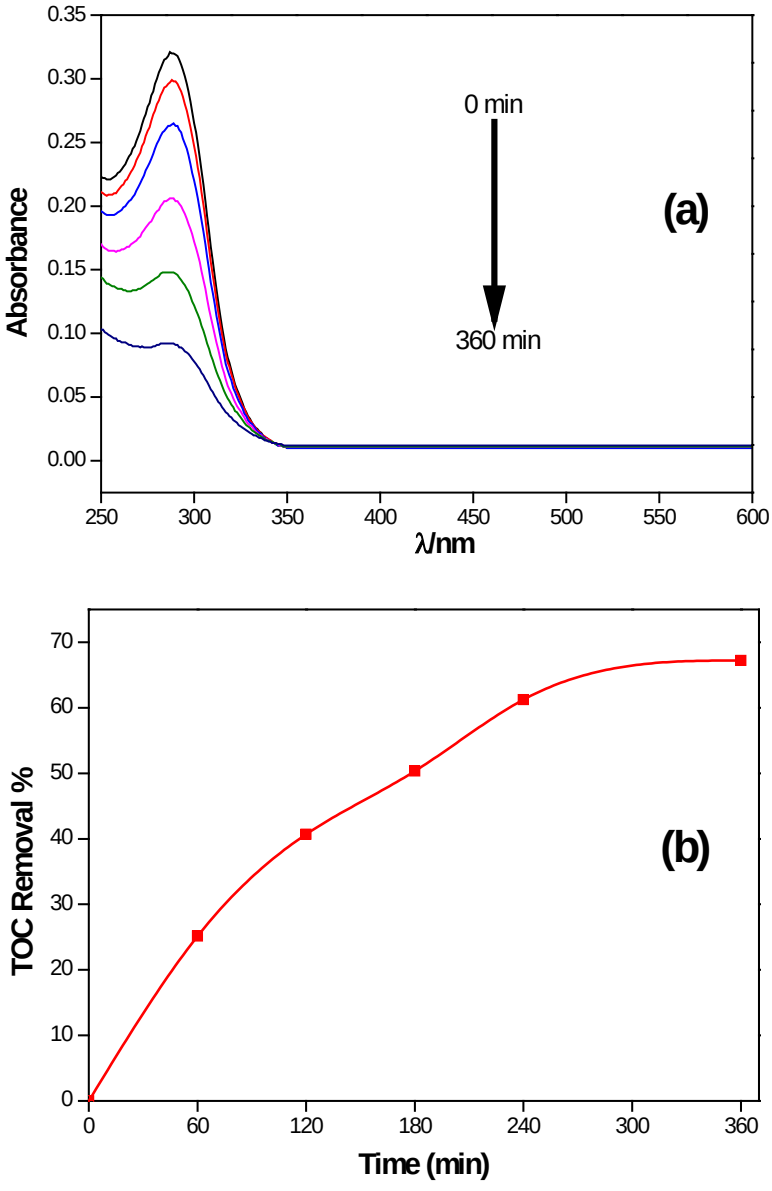

Fig. 2

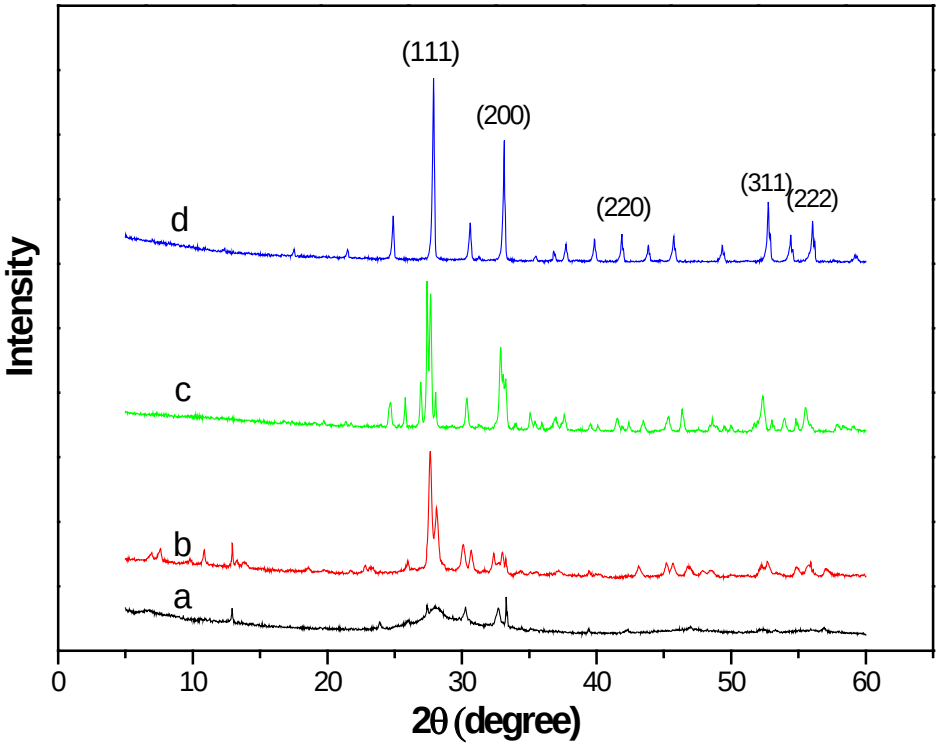

Fig. 3

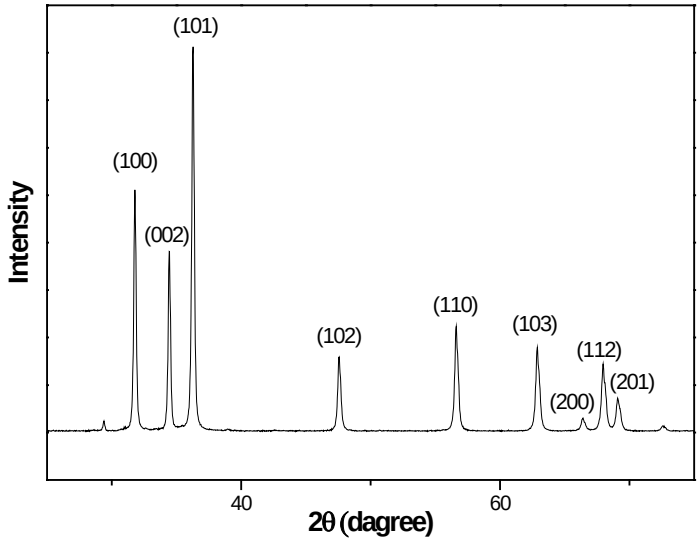

Fig. 4

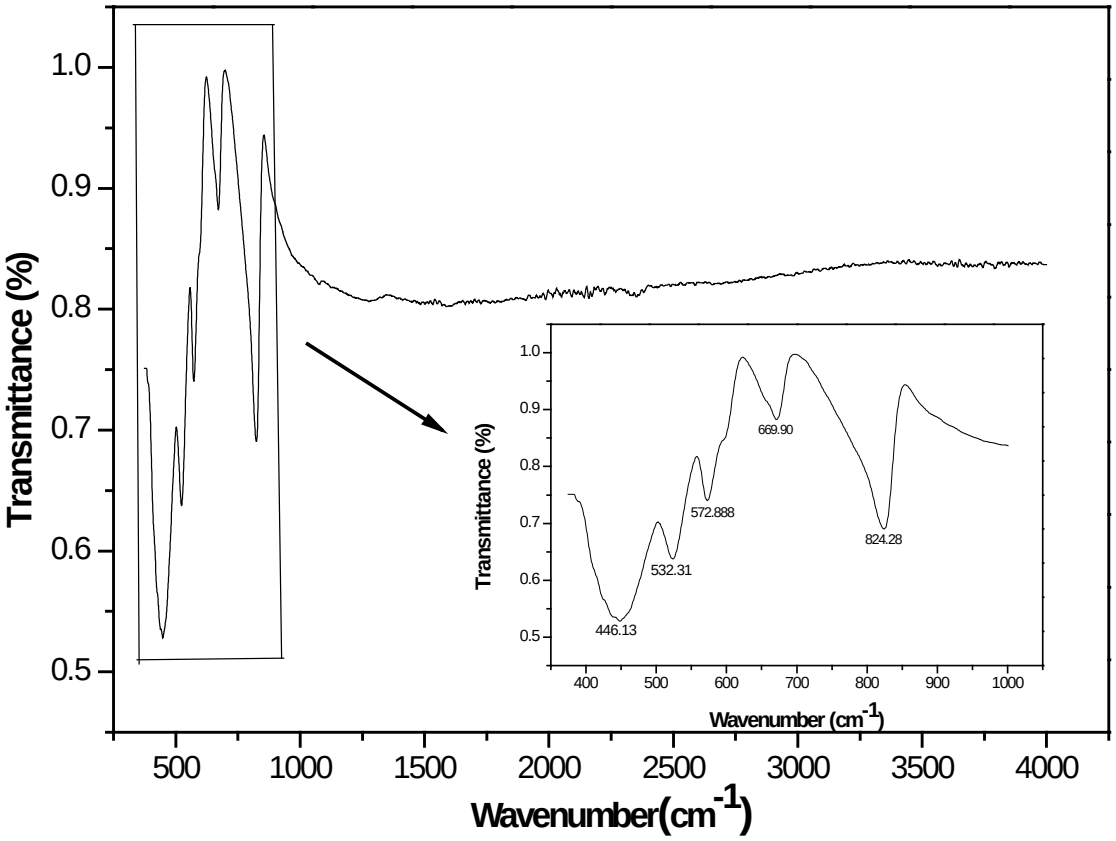

Fig. 5

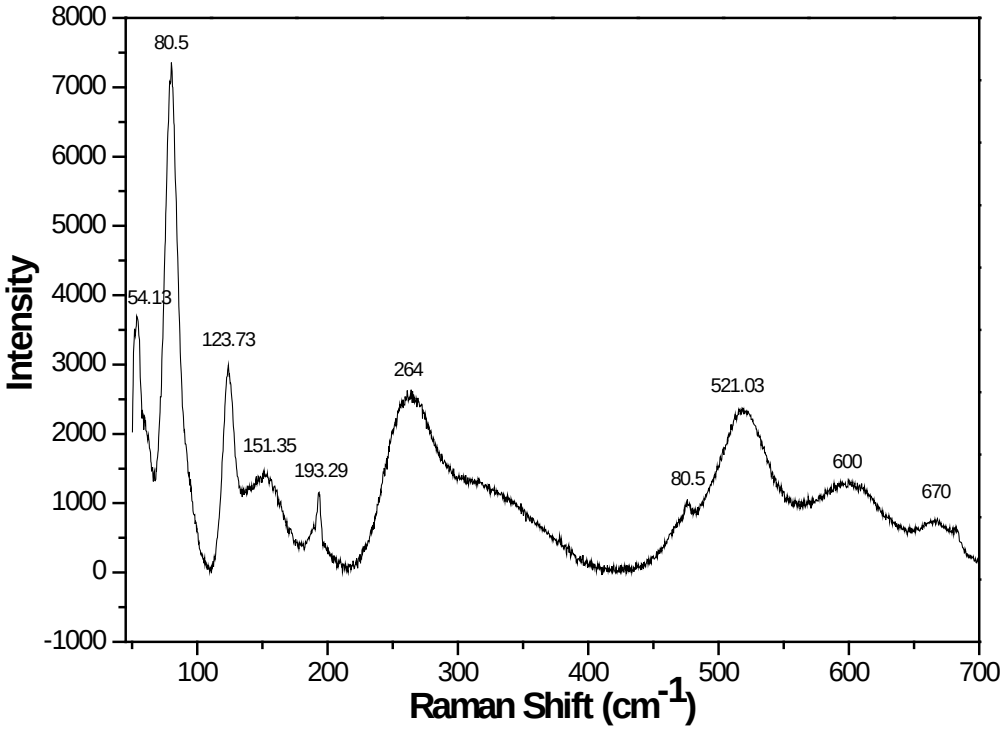

Fig. 6

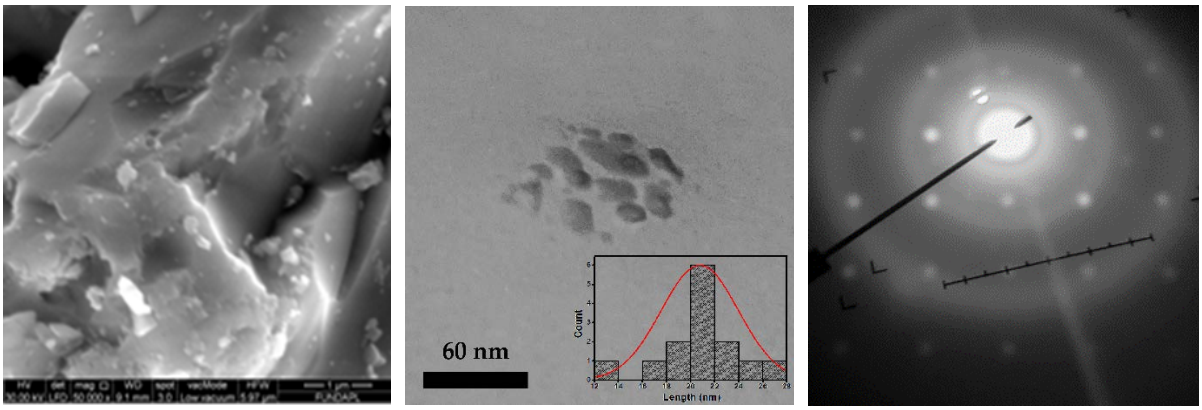

Fig. 7

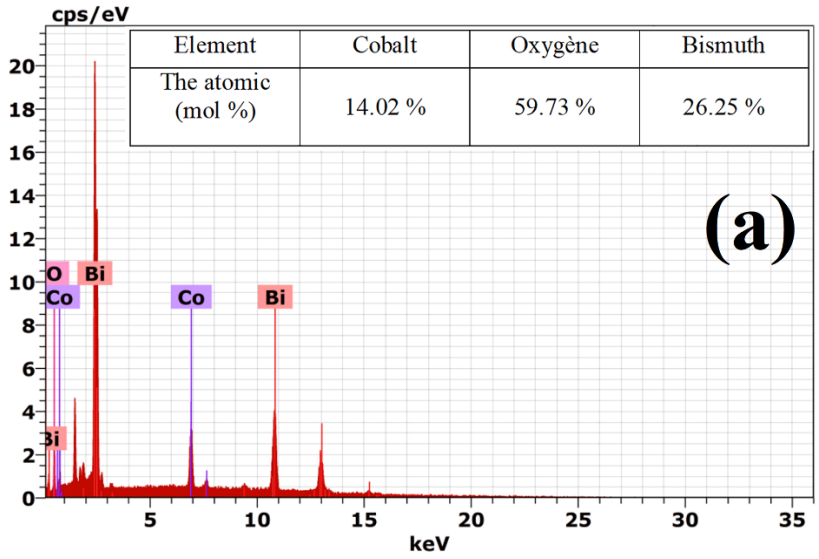

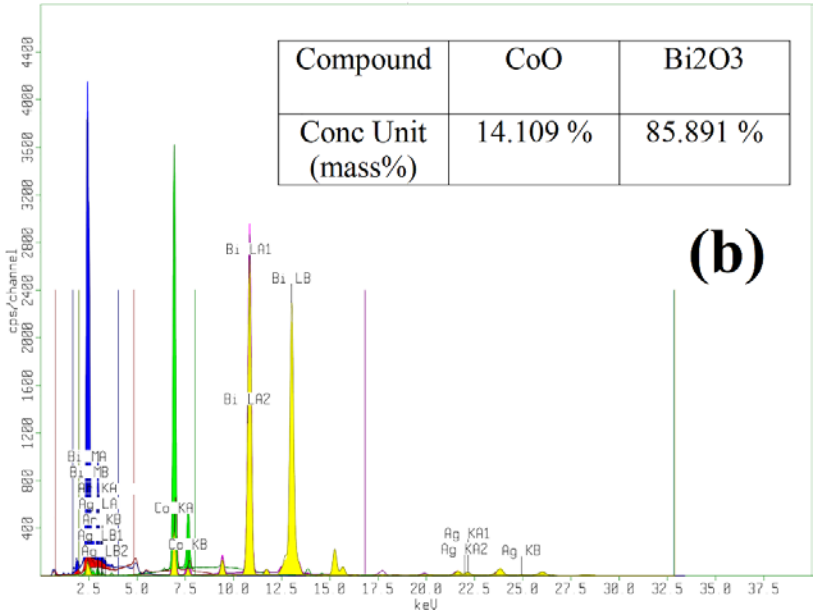

Fig. 8

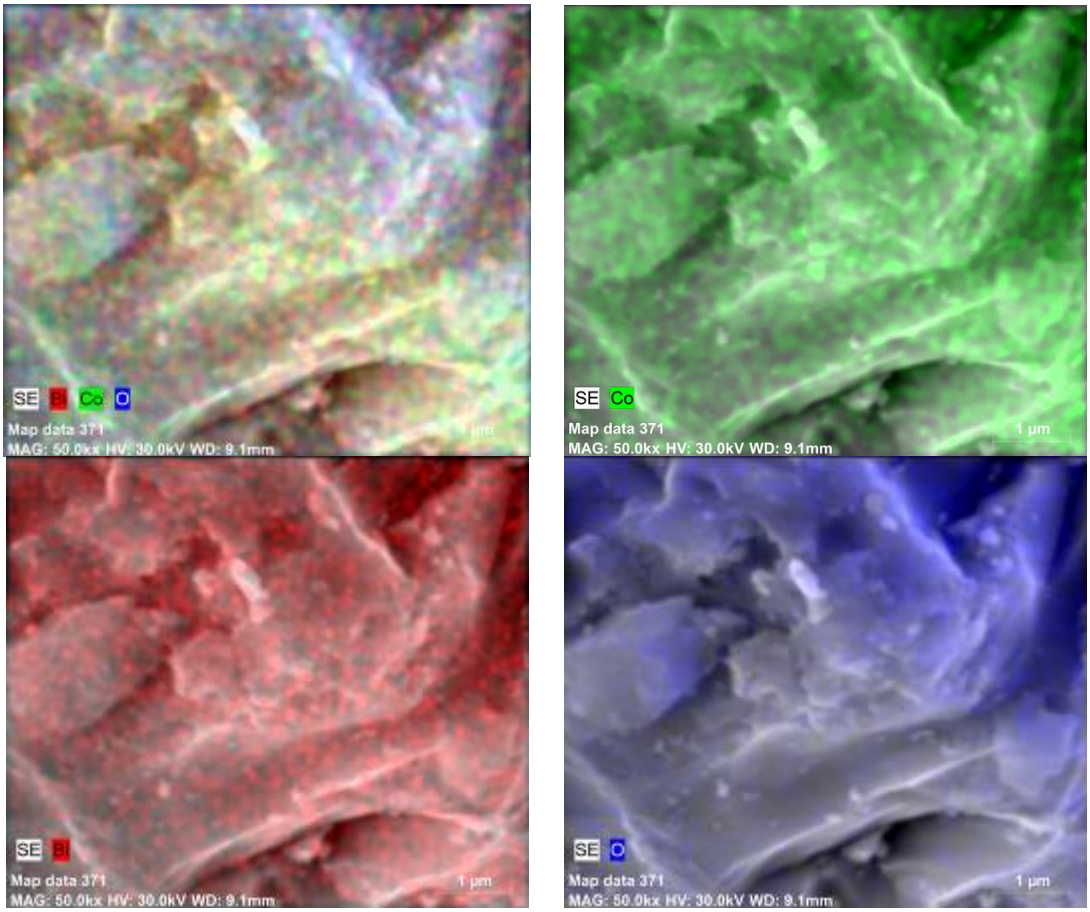

Fig. 9

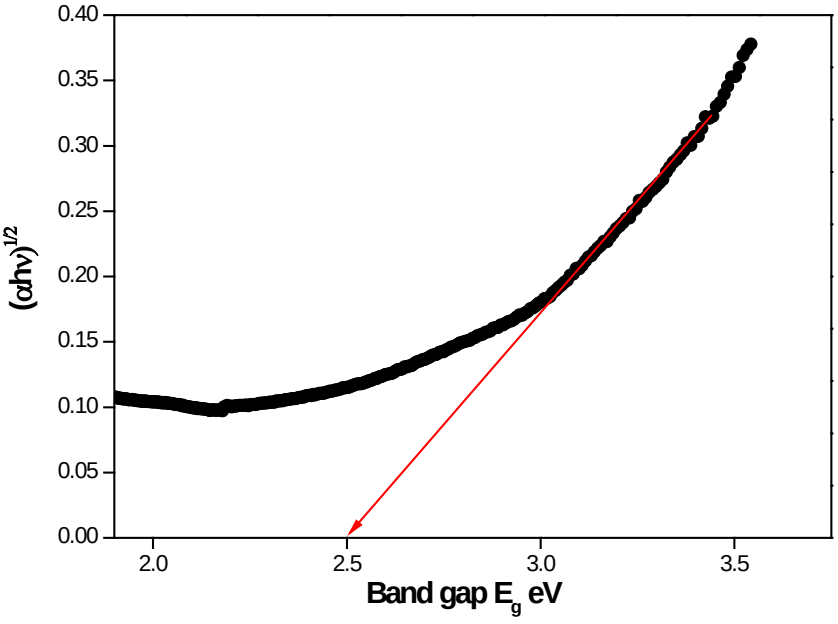

Fig. 10

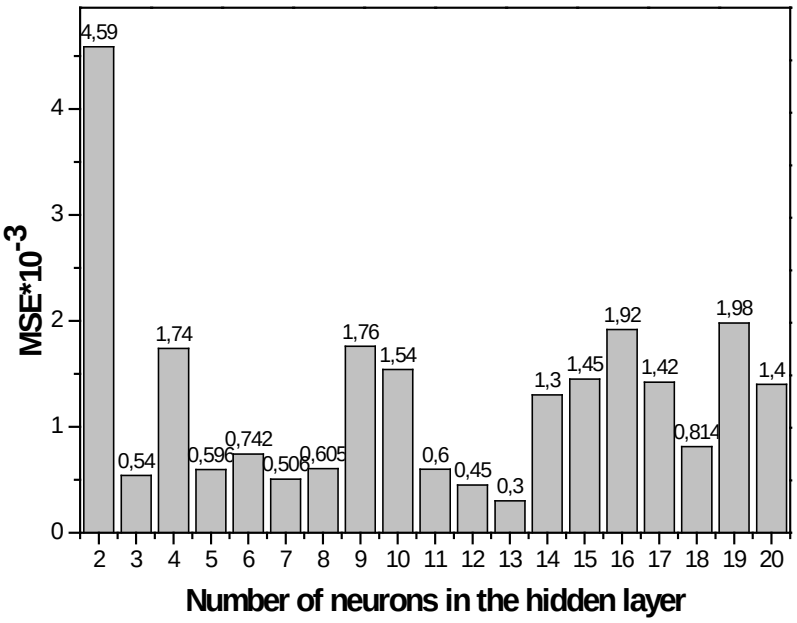

Fig. 11

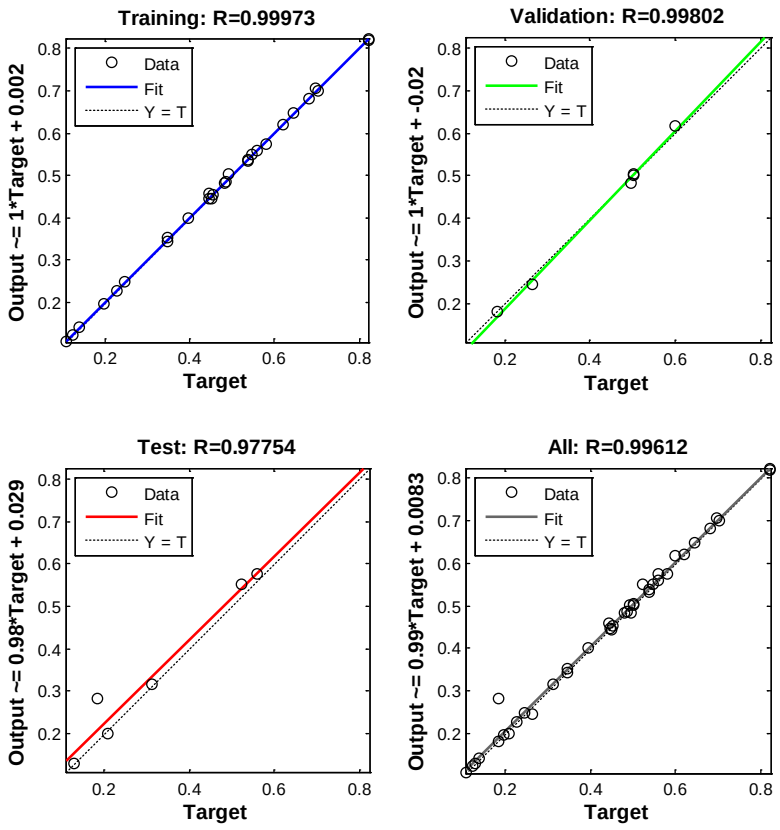

Fig. 12

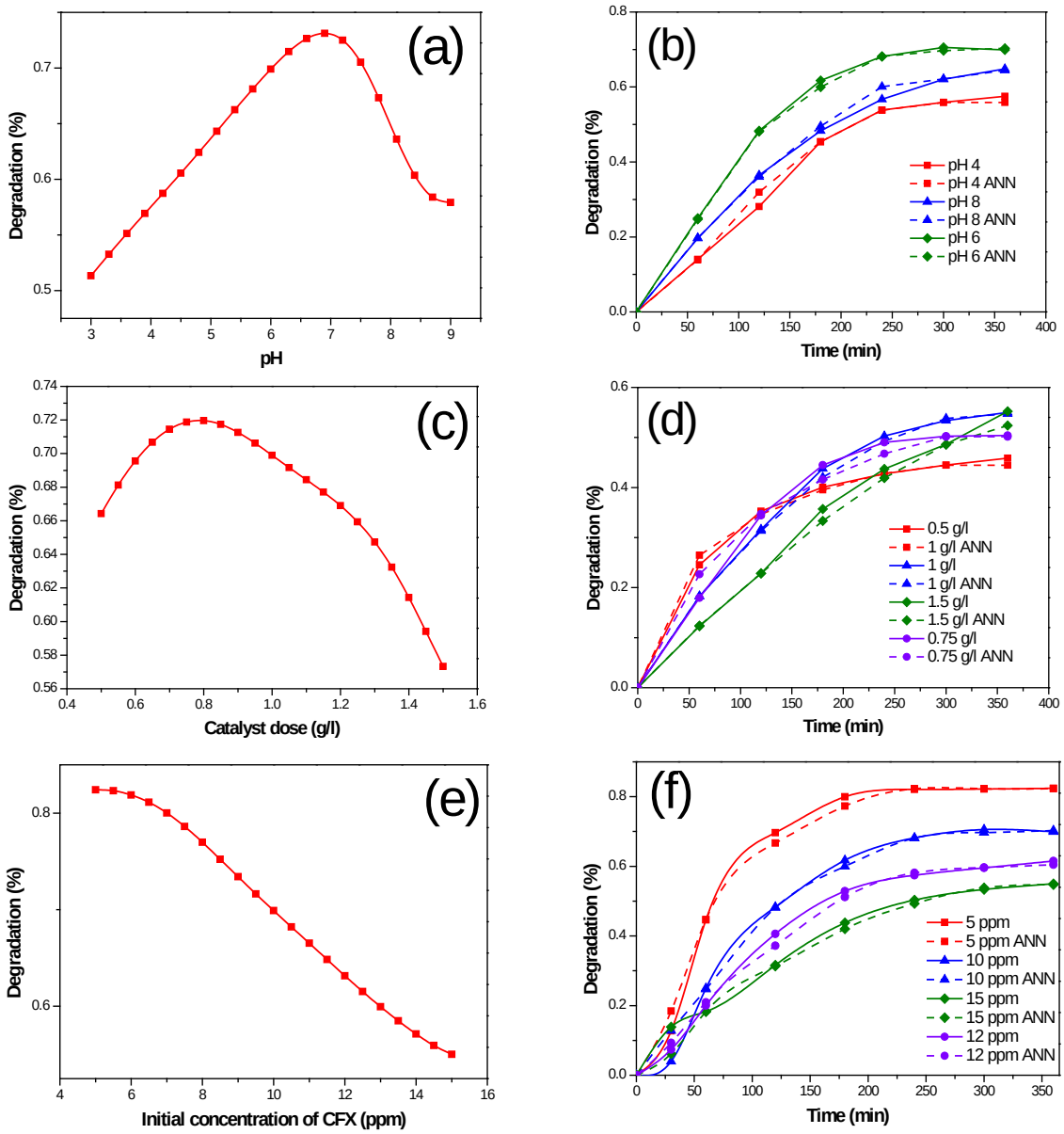

Fig. 13

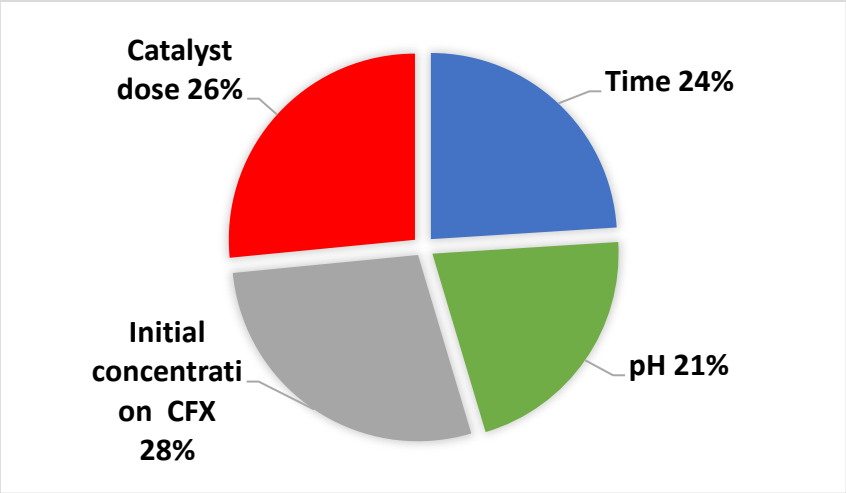

Fig. 14

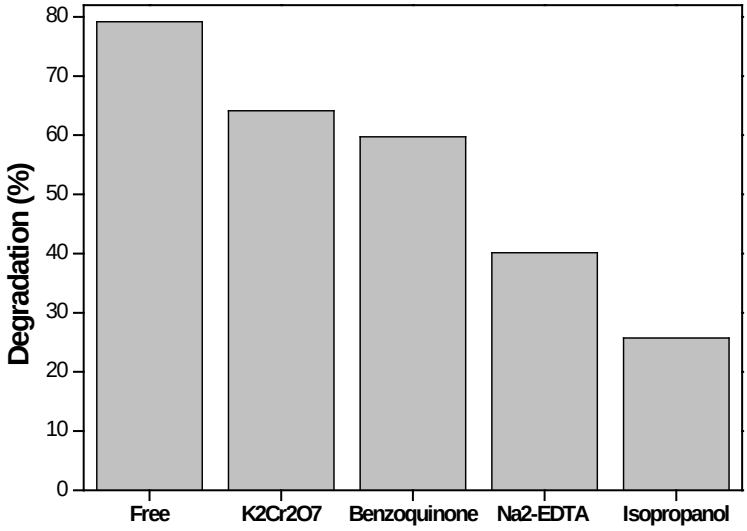

Fig. 15

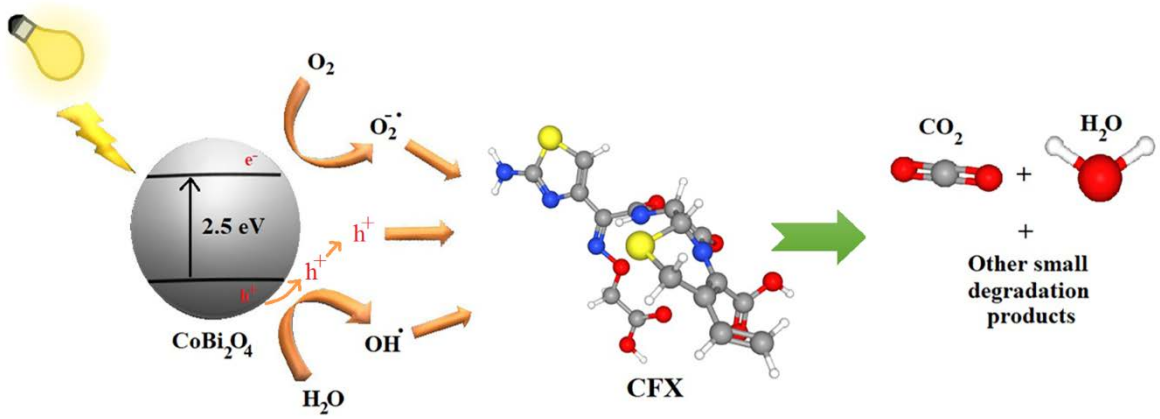

Fig. 16

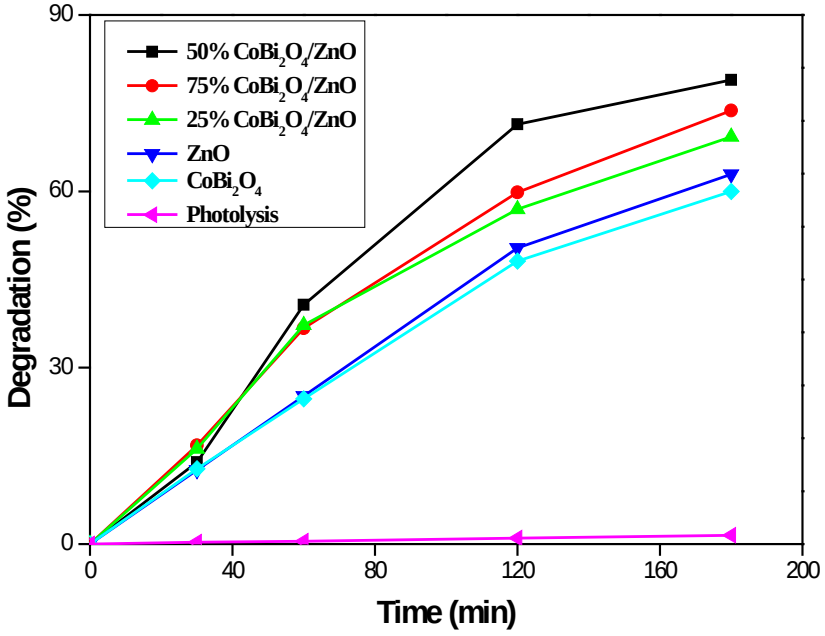

Fig. 17